



Pole identification method to extract the equivalent fluid characteristics of general sound-absorbing materials

Antoni Alomar, Didier Dagna, Marie-Annick Galland *

Universite de Lyon, Ecole Centrale de Lyon, INSA Lyon, UCB Lyon 1, CNRS LMFA, UMR 5509, 36 Av Guy de Collongue, Ecully 69134, France

ARTICLE INFO

Article history:

Received 10 March 2020

Received in revised form 18 October 2020

Accepted 23 October 2020

Available online 22 November 2020

Keywords:

Porous materials

Effective acoustic medium

Partial fraction decomposition

ABSTRACT

A method is presented to characterize general sound-absorbing materials through a pole-based identification of the equivalent fluid. This is accomplished by 1) determining the extended equivalent fluid of the material sample through the transfer function method (TFM), 2) identification of the acoustic response of the material through the poles of the extended effective density and compressibility, and 3) build the effective density and compressibility from the poles associated to the local acoustic response. Real pole pairs describe a dissipative medium (or equivalently an over-damped resonating medium), which is the natural behavior of rigid-frame porous materials, while complex-conjugate pole pairs describe a locally-resonant medium typical of metamaterials. Complex-conjugate poles associated to elastic resonances of the sample are discarded. We test the method for several non-conventional porous materials. In general, a better fit to the measured surface impedance is obtained than with an acoustics-based identification to the Johnson-Champoux-Allard-Pride-Lafarge model (JCAPL), and the method appears also to be robust to errors of the TFM.

© 2020 The Authors. Published by Elsevier Ltd. This is an open access article under the CC BY-NC-ND license (<http://creativecommons.org/licenses/by-nc-nd/4.0/>).

1. Introduction

The increasing global need for diminishing the environmental noise levels pushes the development of materials with improved acoustic performance in multiple applications: architectural acoustics, air conditioning systems, silencers of terrestrial motorized vehicles, ventilation systems, aircraft engine noise, etc. An accurate acoustic modeling of these materials is crucial in order to make predictions in untested configurations, and to implement optimization strategies.

Many sound-absorbing materials behave like an equivalent fluid characterized by an effective density and effective compressibility, which are complex functions of frequency. Based on the physics of acoustic perturbations at the microstructure level followed by homogenization, a number of models for the effective density and effective compressibility have been proposed, such as Attenborough's model [1], the Johnson-Champoux-Allard-Pride-Lafarge model (JCAPL) [2–5], Wilson's relaxational model [6], or the recent three-parameter model of Horoshenkov et al. [7]. All of them rely on a distinct set of physical hypotheses and on a certain knowledge of the geometrical properties of the microstructure.

They are characterized in general by a set of parameters which can be measured through specific tests, like the resistivity [8], porosity [9], tortuosity [10], etc. The validity of the resulting models is then classically verified by acoustic impedance measurements in a Kundt's tube. This process can become complex and long because of the large number of parameters and thus of independent testing rigs, requiring in general multiple samples, whose homogeneity is not guaranteed. This is why many users choose to perform the parameter identification entirely from acoustic measurements in a Kundt's tube, and the parameters are determined from a best-fit of the measured and predicted surface impedance in the frequency range of interest. But this method is not always satisfactory. Besides relying on different physical assumptions which may not be met by certain types of microstructure, it frequently leads to parameter values outside the ranges compatible with their physical grounds.

The concept of equivalent fluid strictly requires that the material sustains a single acoustic wave mode. In the particular case of porous materials this implies that the frame is rigid to acoustic perturbations. But in reality porous materials do not have a rigid frame, even if they can behave as rigid in certain conditions, and the deformation of the frame needs to be accounted in general. In a first approximation, small deformations of the frame can be modelled linearly, leading to the so-called poro-elastic materials. Description of poro-elastic materials requires the full theory of Biot

* Corresponding author.

E-mail addresses: tonignasi@gmail.com (A. Alomar), didier.dragna@ec-lyon.fr (D. Dagna), marie-annick.galland@ec-lyon.fr (M.-A. Galland).

[11–13] in order to account for the coupling of the acoustic field and the elastic frame. For conventional air-saturated porous materials, where the mass density of the frame is much larger than the mass density of air, this coupling is in practice only important in the vicinity of the elastic resonances of the sample [14]. Away from the resonances the material behaves close to the rigid-frame limit. However, the high sensitivity of the resonant response to the sample boundary conditions, together with the difficulty of determining the exact experimental boundary conditions, make impractical a direct identification to the full poro-elastic model.

Double porosity materials are another example of materials beyond the scope of existing equivalent fluid models. These materials are composed of a microstructure and a mesostructure: a number of inclusions of a secondary material are embedded inside the primary microstructure. The models of the microstructure and the mesostructure need to be appropriately coupled, which in general depends on the particular geometry of the inclusions. In the simple case of cylindrical inclusions under normal incidence, an analytical coupling model has been proposed [15].

Locally-resonant acoustic metamaterials have been widely studied in the last two decades due to their high absorption potential. This type of metamaterials are characterized by local/inner resonances which can absorb incoming acoustic energy [16]. These local resonances can induce a negative effective density [17–19] and/or negative effective compressibility [20,21] (real parts) in certain frequency bands, leading to an imaginary sound speed and no propagation of sound there. These materials are not found in nature but can be manufactured artificially. The continuous improvement of fabrication technologies will soon allow to manufacture locally-resonant metamaterials with optimal absorption properties [22]. Although simple equivalent fluid models exist around the local resonances [23], no general physical model exists for these materials.

The transfer function method (TFM) [24] can be used to determine the equivalent fluid of any given material sample. TFM was originally proposed for porous materials, but it can be applied to any material that can be acoustically described through an equivalent fluid. As the concept of equivalent fluid, TFM assumes there is a single acoustic plane wave mode in the material, for which reason it is conventionally restricted to rigid-frame porous materials. Nevertheless, it can in principle be applied to more general materials, in which case the deduced equivalent fluid needs to be interpreted appropriately.

The fast development of 3D-printing technology allows nowadays to fabricate rigid porous networks with a deterministic microstructure [25]. However, the pore sizes are still limited to the order of millimeters, which is significantly larger than the wavelengths of interest in acoustics, but may be of the order of the sample sizes used. Even if these rigid-frame, porous-like materials are strictly described by JCAPL [26], the use of samples of material which are not large enough (compared to the microstructure characteristic length), may induce errors in the determination of the equivalent fluid through TFM.

A new identification approach is proposed here based on a pole identification of the effective density and compressibility determined from TFM, thus relying only on acoustic measurements of a single material sample. First, a partial fraction expansion is fitted to the effective density and compressibility obtained from TFM. And second, the real and complex-conjugate poles in the expansion are identified to certain physical behaviors of sound propagation in the material, including dissipative, local resonances, or sample resonances. Therefore, the model proposed allows to characterize not only rigid-frame porous materials, but also poro-elastic materials, double-porosity materials and metamaterials. The sample reso-

nances can then be discarded to obtain the equivalent fluid characteristics of the material.

From a practical standpoint the method used is similar to an acoustic JCAL identification, but it has the advantage that it benefits from vector fitting [27] or Padé approximants [28] to determine the optimum pole parameters. In a JCAPL identification the parameters are determined by a generic minimization algorithm, in general less efficient.

Finally, another advantage of the proposed identification method has to do with its relationship with the formulation of sound propagation in the time-domain. Using the Additional Differential Equation (ADE) method [29], a pole-based model of the effective medium leads to a time-domain formulation of the propagation of acoustic waves through the material. As opposed to other methods, this approach is compatible with high-order numerical schemes [30].

After describing the method in Sections 2–4, in Section 5 we validate it and compare it against an acoustic-based JCAPL identification, for various conventional and non-conventional porous materials: a melamine sample, a rock wool exhibiting an acoustic-elastic coupling, a double-porosity rock wool sample, and two 3D-printed porous networks with a large pore size.

2. Extended equivalent fluid

We define an extended equivalent fluid as the effective density, $\tilde{\rho}_{ext}$, and the effective compressibility, \tilde{K}_{ext}^{-1} , leading to the correct acoustic field outside the material when modelled through the equations (using the $\exp(j\omega t)$ convention):

$$j\omega\tilde{\rho}_{ext}(\omega)\hat{u} + \frac{\partial\hat{p}}{\partial x} = 0, \quad (1)$$

$$j\omega\tilde{K}_{ext}^{-1}(\omega)\hat{p} + \frac{\partial\hat{u}}{\partial x} = 0, \quad (2)$$

where \hat{p} and \hat{u} are the temporal Fourier transforms of the pressure and the velocity fields, respectively. These equations need to be accompanied by the appropriate acoustic boundary conditions. The extended effective speed of sound in the material is then:

$$\tilde{c}_{ext}(\omega) = \sqrt{\frac{\tilde{K}_{ext}(\omega)}{\tilde{\rho}_{ext}(\omega)}}, \quad (3)$$

and the extended characteristic impedance and propagation wavenumber can be expressed as:

$$\tilde{Z}_{ext}(\omega) = \sqrt{\tilde{\rho}_{ext}(\omega)\tilde{K}_{ext}(\omega)}, \quad (4)$$

$$\tilde{k}_{ext}(\omega) = \omega \sqrt{\frac{\tilde{\rho}_{ext}(\omega)}{\tilde{K}_{ext}(\omega)}}. \quad (5)$$

Consider a sample of material of thickness H_m in a duct. The surface impedance corresponding to a rigid-backing and a configuration with an air gap of depth L_{ag} are, respectively:

$$Z_s(\omega) = -j \frac{\tilde{Z}_{ext}(\omega)}{\phi} \cot(\tilde{k}_{ext}(\omega)H_m), \quad (6)$$

$$Z_{s,ag}(\omega) = \frac{\tilde{Z}_{ext}(\omega) - \phi \cot(\omega H_m L_{ag}/c_0) \cot(\tilde{k}_{ext}(\omega)H_m) + \tilde{Z}_{ext}(\omega)}{\phi \left[-j\phi \cot(\omega H_m L_{ag}/c_0) + j\tilde{Z}_{ext}(\omega) \right]}, \quad (7)$$

where ϕ is the porosity of the material. The absorption coefficient is then determined directly from either surface impedance as:

$$\alpha = 1 - \left| \frac{Z_s - \rho_0 c_0}{Z_s + \rho_0 c_0} \right|^2. \quad (8)$$

Eqs. (1) and (2) imply that there is a single wave mode in the material which obeys the acoustic boundary and interface conditions. If there are more than one wave modes, as in the case of poro-elastic materials, the acoustic wave mode is interpreted as an *equivalent acoustic wave mode* leading to the correct acoustic field outside the material. In general, the extended equivalent fluid of a material sample cannot be regarded as an actual equivalent fluid because it depends on the sample dimensions and boundary conditions, and not only on the material itself. The effective density and compressibility of an actual equivalent fluid model are labelled $\tilde{\rho}$, and \tilde{K}^{-1} .

2.1. Relationship between the extended equivalent fluid and TFM

The TFM [24] unveiled a correspondence between the effective density and compressibility of a given porous material sample and its surface impedance corresponding to two different rear boundary conditions, and provided an experimental procedure to determine $\tilde{\rho}$ and \tilde{K}^{-1} . The TFM equations are a direct consequence of Eqs. 1.2 and the boundary and interface conditions, and they have the same assumptions: there is a single wave mode propagating in the material which obeys the acoustic boundary and interface conditions, leading to the correct acoustic field outside the material. This is why the output of TFM can actually be interpreted as an extended effective density and compressibility. Furthermore, the generality of the extended equivalent fluid concept allows the application of TFM not only to porous, but also to other types of sound absorbing materials. In the identification method proposed, TFM is used to determine the extended effective density and extended effective compressibility of the samples of sound-absorbing material.

3. Pole-based model of the equivalent fluid

In this section we present a method to characterize and extract the equivalent fluid from the extended equivalent fluid. First we show how the poles of the extended effective density and compressibility determined from TFM can be determined efficiently using a partial fraction expansion. Then we present the physical interpretation of the poles, including the poles associated to the elastic resonances of the sample. Finally, a summary of the process to extract the equivalent fluid model of a given material sample is presented.

3.1. Partial fraction expansion of the extended equivalent fluid

The extended effective density and extended effective compressibility obtained from TFM can be decomposed as a sum of real and complex poles through a partial fraction expansion:

$$\tilde{\rho}_{ext}(\omega) = \rho_{e\infty} + \sum_{k=1}^{Nr\rho} \frac{A_{\rho k}}{\lambda_{\rho k} - j\omega} + \sum_{l=1}^{Ni\rho} \left(\frac{B_{\rho l} + jC_{\rho l}}{\alpha_{\rho l} + j\beta_{\rho l} - j\omega} + \frac{B_{\rho l} - jC_{\rho l}}{\alpha_{\rho l} - j\beta_{\rho l} - j\omega} \right) \quad (9)$$

$$\tilde{K}_{ext}^{-1}(\omega) = K_{e\infty}^{-1} + \sum_{k=1}^{Nrc} \frac{A_{c k}}{\lambda_{c k} - j\omega} + \sum_{l=1}^{Nic} \left(\frac{B_{c l} + jC_{c l}}{\alpha_{c l} + j\beta_{c l} - j\omega} + \frac{B_{c l} - jC_{c l}}{\alpha_{c l} - j\beta_{c l} - j\omega} \right), \quad (10)$$

where the complex poles come in complex-conjugate pairs because the inverse Fourier transform of $\tilde{\rho}_{ext}(\omega)$ and $\tilde{K}_{ext}^{-1}(\omega)$ must be real. There exist various algorithms in the literature to determine the

optimal pole parameters for given $\tilde{\rho}_{ext}(\omega)$ and $\tilde{K}_{ext}^{-1}(\omega)$, such as vector fitting [27] or the Padé approximants [28]. In order that all solutions are stable all the poles of $\tilde{\rho}_{ext}$ and \tilde{K}_{ext}^{-1} need to have positive real values of λ_i and α_i , which is not an issue because both algorithms allow to search for stable poles only. Vector fitting has been used here.

Since the number of poles is an input to the vector fitting algorithm, the question then arises of whether to directly fit with a small number of poles or fitting with a larger number of poles, and then retain the desired poles. In all cases tested the difference between both cases is small. The results shown correspond to fitting with a reduced number of poles.

3.2. Local effective response: dissipative and resonant

The physical grounds for using real and complex-conjugate pole pairs of the effective density and effective compressibility to describe an equivalent fluid are taken from the theory of metamaterials. According to effective medium theory arguments in electromagnetic metamaterials, together with the electromagnetic-acoustic analogy, a locally-resonant acoustic metamaterial can be modelled by a continuous distribution of harmonic oscillators leading to an effective compressibility of the form [31,32,23,20]:

$$\tilde{K}^{-1}(\omega) \approx \frac{1}{\rho_0 c_0^2} - \frac{F_c \omega_{s_c}^2 - j\omega \omega_{s_c} G_c}{\omega^2 - \omega_{s_c}^2 - j\Gamma_c \omega}, \quad (11)$$

where ω_{s_c} and Γ_c are the natural resonance frequencies of the effective medium and their damping coefficients, respectively. An additional derivative forcing term (which is zero in the metamaterial literature) has been added in the numerator, and will be justified later. An analogous expression can be supposed for the effective density:

$$\tilde{\rho}(\omega) \approx \rho_0 - \frac{F_\rho \omega_{s_\rho}^2 - j\omega \omega_{s_\rho} G_\rho}{\omega^2 - \omega_{s_\rho}^2 - j\Gamma_\rho \omega}. \quad (12)$$

As simple examples, a 1D duct coupled to a continuous distribution of Helmholtz resonators is equivalent to an effective medium defined by Eq. (11) [23,21], and this is also the case of a layered composite material [33]. On the other hand, a duct filled with a distribution of membranes is equivalent to an effective medium defined by Eq. (12) [19,21].

Eqs. (11) and (12) lead to two different behaviors depending on the relative value of the dissipation and the resonant frequency: over-damped and under-damped.

3.2.1. Dissipative behavior: real pole pairs

In the case of an equivalent fluid associated to $\tilde{\rho}$ (an analogous argument applies to \tilde{K}^{-1}), if $\Gamma_\rho > 2\omega_{s_\rho}$ the resonance is over-damped, and the resonator is equivalent to a pair of real poles:

$$\tilde{\rho}(\omega) = \rho_0 + \frac{A_{\rho 1}}{\lambda_{\rho 1} + j\omega} + \frac{A_{\rho 2}}{\lambda_{\rho 2} + j\omega}, \quad (13)$$

$$\lambda_{\rho 1} = \frac{-\Gamma_\rho - \sqrt{\Gamma_\rho^2 - 4\omega_{s_\rho}^2}}{2}, \quad \lambda_{\rho 2} = \frac{-\Gamma_\rho + \sqrt{\Gamma_\rho^2 - 4\omega_{s_\rho}^2}}{2}, \quad (14)$$

$$A_{\rho 1} = \frac{F_\rho \omega_{s_\rho}^2 - \lambda_{\rho 2} \omega_{s_\rho} G_\rho}{\sqrt{\Gamma_\rho^2 - 4\omega_{s_\rho}^2}}, \quad A_{\rho 2} = \frac{-F_\rho \omega_{s_\rho}^2 - \lambda_{\rho 1} \omega_{s_\rho} G_\rho}{\sqrt{\Gamma_\rho^2 - 4\omega_{s_\rho}^2}}. \quad (15)$$

In this case the dissipation overwhelms the underlying resonant behaviour. Note that the additional terms G_ρ, G_c in Eqs. 11,12 allow that $A_{\rho 1} + A_{\rho 2} \neq 0, A_{c 1} + A_{c 2} \neq 0$, leading to a more general real pole pair (as in Eq. (9)).

All rigid-frame porous materials obeying JCAPL appear to be well-described using a reduced number of real poles for the effective

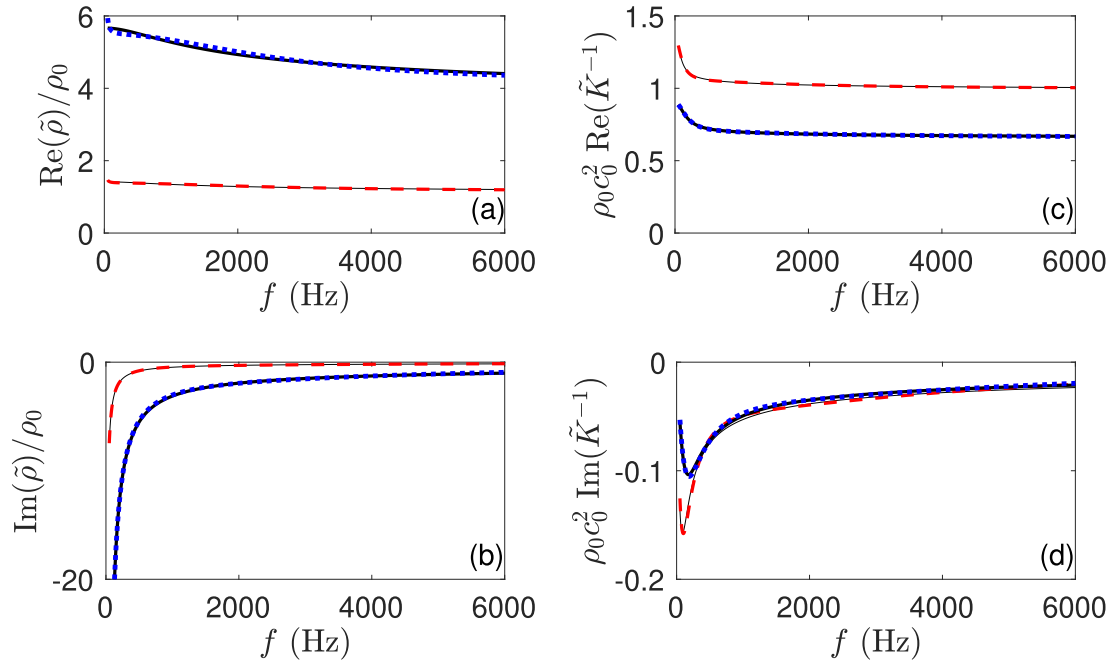


Fig. 1. JCAL prediction of the effective density (a,b) and the effective compressibility (c,d) of a rigid-frame polyurethane foam with $\sigma = 2850 \text{ N}\cdot\text{s}\cdot\text{m}^{-4}$ (—), and a rigid-frame metallic foam with $\sigma = 19200 \text{ N}\cdot\text{s}\cdot\text{m}^{-4}$ (—), reconstruction using one pair of real poles of the polyurethane foam (- - -), and the metallic foam (■ ■).

tive density and effective compressibility. Fig. 1 shows the fit for two rigid-frame foams of low resistivity ($\phi = 0.98$, $\alpha_\infty = 1.04$, $\sigma = 2850 \text{ N}\cdot\text{s}\cdot\text{m}^{-4}$, $\Lambda = 2 \cdot 10^{-4} \text{ m}$, $\Lambda' = 5 \cdot 10^{-4} \text{ m}$) [34] and moderate resistivity ($\phi = 0.65$, $\alpha_\infty = 2.25$, $\sigma = 19700 \text{ N}\cdot\text{s}\cdot\text{m}^{-4}$, $\Lambda = 1 \cdot 10^{-4} \text{ m}$, $\Lambda' = 3.5 \cdot 10^{-4} \text{ m}$) [35], using one real pole pair. More real poles may be added for higher accuracy or if a larger frequency band is considered.

3.2.2. Locally-resonant behavior: complex-conjugate pole pairs

On the other hand, if the resonance is under-damped, i.e. $\Gamma_\rho < 2\omega_{* \rho}$, the resonator is equivalent to a pair of complex conjugate poles:

$$\tilde{\rho}(\omega) = \rho_0 + \frac{B_\rho + jC_\rho}{\alpha_\rho + j\beta_\rho + j\omega} + \frac{B_\rho - jC_\rho}{\alpha_\rho - j\beta_\rho + j\omega}, \quad (16)$$

$$\alpha_\rho = -\frac{\Gamma_\rho}{2}, \quad \beta_\rho = \frac{\sqrt{-\Gamma_\rho^2 + 4\omega_{* \rho}^2}}{2}, \quad (17)$$

$$B_\rho = \frac{\omega_{* \rho} G_\rho}{2}, \quad C_\rho = \frac{F_\rho \omega_{* \rho}^2 - \alpha_\rho \omega_{* \rho} G_\rho}{\sqrt{-\Gamma_\rho^2 + 4\omega_{* \rho}^2}},$$

and in this case the equivalent fluid responds to an impulsive source as a damped resonator at its natural frequency, $\omega_{* \rho}$. Note that the additional terms G_ρ, G_c in Eqs. ((11) and (12)) allow that $B_\rho \neq 0, B_c \neq 0$, leading to a general complex-conjugate pole pair (as in Eq. (9)). This locally-resonant behavior, described through a complex-conjugate pole pair of the equivalent fluid, is associated to metamaterials. For frequencies where $\text{Re}(\tilde{\rho}) < 0$ or $\text{Re}(\tilde{K}^{-1}) < 0$ the sound velocity (Eq. (3)) becomes purely imaginary and plane waves decay exponentially. In the even more peculiar, but realizable case that $\text{Re}(\tilde{\rho}) < 0$ and $\text{Re}(\tilde{K}^{-1}) < 0$, the sound velocity is real and plane waves propagate. However, the effective medium response is anomalous: it expands under a pressure rise and moves to the right when pushed to the left (and viceversa) [36].

3.3. Elastic resonances of the sample

Once the poles of the extended equivalent fluid have been identified from a partial fraction expansion of $\tilde{\rho}_{\text{ext}}$ and $\tilde{K}_{\text{ext}}^{-1}$, only the ones associated to the local acoustic response should be retained in the equivalent fluid model of the material. The poles associated to resonances of the sample, as the ones usually appearing in poro-elastic materials, are discarded. As will be shown in Section 5.2, the surface impedance around the elastic resonances is well captured by a real pole pair plus a complex-conjugate pole pair of $\tilde{\rho}_{\text{ext}}$ and $\tilde{K}_{\text{ext}}^{-1}$. An analytical justification for this is hard to find from the full poro-elastic model, mainly because the two wave modes in the material are important and neither can be directly identified with an elastic mode or an acoustic mode. However, an argument can be made to justify the apparent simplicity observed. Consider an elementary mechanical model (EMM) of the elastic sample consisting of a two-degree-of-freedom mass-spring-damper, characterized by a mass m_* , a damper of constant χ_* and a spring of constant k_* , as shown in Fig. 2. As the excitation is harmonic ($\sim \exp(j\omega t)$) so is the resulting acoustic field and the vibration of the EMM. The acoustic field in the duct is equal to:

$$\tilde{p}(x) = A \exp(jkx) + B \exp(-jkx), \quad (18)$$

where A is the amplitude of the incoming wave and B the amplitude of the reflected wave. The external forcing on the EMM is equal to the pressure in the duct at $x = 0$, i.e. $\hat{F}_a = A + B$. The acoustic velocity at $x = 0$ is equal to the velocity of the massless piston, $\hat{u}_a = -(A - B)/(\rho_0 c_0)$. The surface impedance of the EMM is:

$$Z_{s*} = -\frac{\hat{F}_a}{\hat{u}_a} = \rho_0 c_0 \frac{A + B}{A - B}. \quad (19)$$

The application of the force/velocity relations for the spring and the damper, plus Newton's law for the mass leads to the impedance of the EMM [37]:

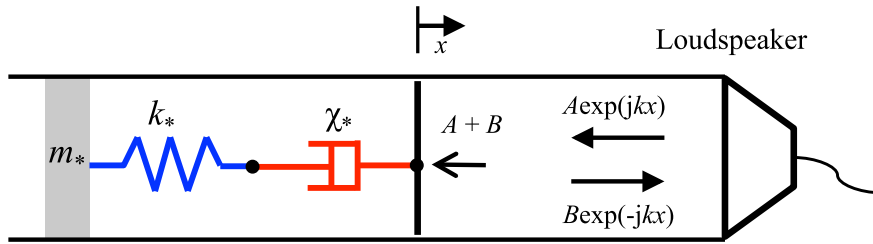


Fig. 2. EMM for the elastic resonances of the sample.

$$Z_{s*} = \frac{j\omega k_*}{-\omega^2 + \frac{k_*}{m_*} + j\omega \frac{\chi_*}{m_*}} \quad (20)$$

The choice of the two-degree-of-freedom mass-spring-damper instead of the conventional one-degree-of-freedom configuration [38] responds to the presence of two wave modes in the material, and will be evident in Section 5.2 from the measured surface impedance. In the proposed analogy, the degree of freedom at $x = 0$ can be associated to the movement of the air, which has a negligible mass, while the degree of freedom of the mass element can be associated to the vibration of the frame. This type of resonance is similar to the mass-air-mass resonance encountered for example in double-glazed windows [39].

Now that we have put forward a model for the acoustic impedance associated to the elastic resonances, can we identify it with a complex-conjugate pole pair of $\tilde{\rho}_{ext}$ and \tilde{K}_{ext}^{-1} ? Using Eqs. (6), (16) and (13) to compute the surface impedance associated to a complex-conjugate pole pair of $\tilde{\rho}_{ext}$ and/or \tilde{K}_{ext}^{-1} , it is observed that it indeed creates a complex-conjugate pole pair of the surface impedance, as in Eq. (20), but also introduces a pair of real poles, due to the divergence of the cotangent at low frequencies. This behavior is not accounted by the simple EMM model. Nevertheless, the contribution of the complex-conjugate pole pair on the impedance can be obtained by subtracting the surface impedance component associated to the real pole pair to the total surface impedance:

$$Z_{s*} = Z_s - Z_s^{real \text{ poles}}, \quad (21)$$

where $Z_s^{real \text{ poles}}$ is obtained from Eqs. (6) and (7) retaining only the real poles and the constant term of $\tilde{\rho}_{ext}$ and \tilde{K}_{ext}^{-1} . The resulting impedance contribution due to the elastic resonance should then approach Eq. (20).

Since local and sample resonances may look similar in the extended effective density and compressibility, some *a priori* knowledge of the nature of the material and the boundary conditions, such as the elastic bulk modulus, may be helpful to identify the sample resonances. In the case of conventional porous materials where no local resonances are expected, the complex-conjugate poles can be directly identified to elastic resonances of the sample. Another way to identify the elastic sample resonances is to slightly modify the boundary conditions of the sample in the Kundt's tube. A large impact on the surface impedance around the resonance is indication of a sample resonance.

3.4. Summary of the method to extract the equivalent fluid

In summary, the procedure proposed to determine experimentally the equivalent fluid is composed of three successive steps:

1. experimental determination of the extended equivalent fluid, $\tilde{\rho}_{ext}, \tilde{K}_{ext}^{-1}$, through TFM,

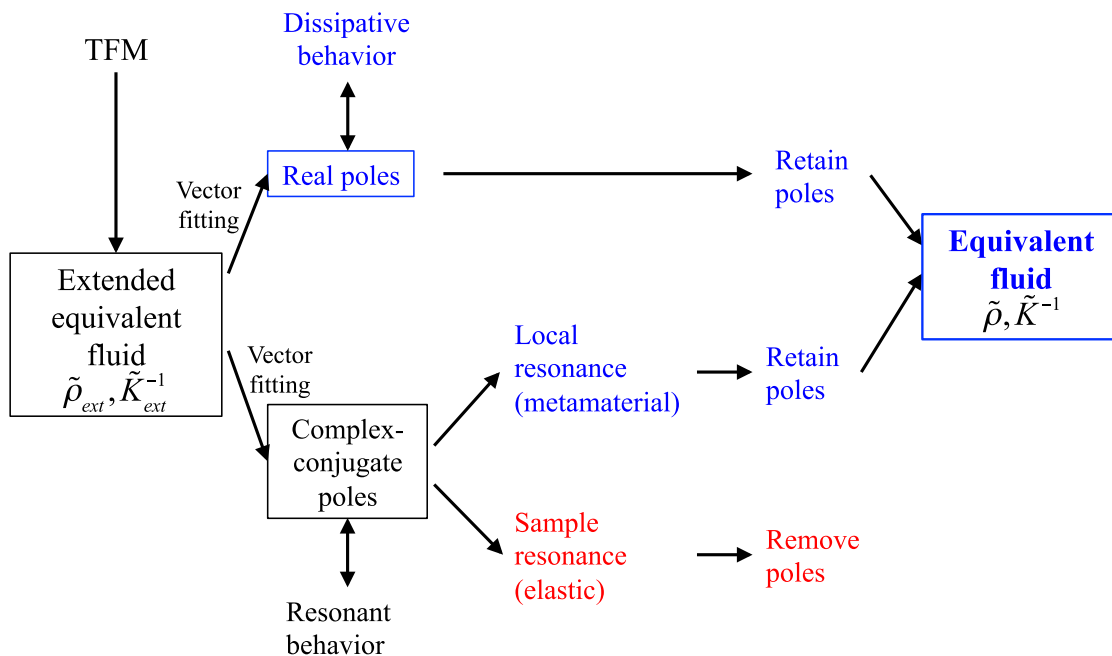


Fig. 3. Conceptual map leading to the choice of real and complex-conjugate pole pairs to build the equivalent fluid model, according to their dissipative/resonant and local/sample nature.

2. identify the pole pairs of $\tilde{\rho}_{ext}, \tilde{K}_{ext}^{-1}$ via partial fraction expansion,
3. identify the sample resonances and build the equivalent fluid of the material, $\tilde{\rho}, \tilde{K}^{-1}$, by superposing the pole pairs describing the local acoustic response of the material, dissipative (real pole pairs) or resonant (complex-conjugate pole pairs).

Fig. 3 shows a conceptual map of the entire procedure to extract the equivalent fluid.

4. Experimental methods

In this section the experimental methodology to characterize the material samples is presented, including the description of

the samples, the TFM method and the complementary JCAPL identification.

4.1. Material samples

We have tested the proposed method against several conventional and non-conventional porous materials:

- (a) As a case of approximately rigid-frame porous material a sample of melamine foam of thickness equal to 30 mm has been tested in a small Kundt's tube ($D = 30$ mm).
- (b) We have tested three samples of a 30 mm thickness rock wool layer exhibiting elastic behavior. The first sample contains no perforations (RW), the second sample (RW-7) and the third

Table 1
Properties of the material samples tested.

Porous material	H_m (m)	D (m)	Frequencies (Hz)	Expected elastic behavior	Double-porosity
Melamine	0.03	0.03	200–5500	Yes	No
RW	0.03	0.10	150–1900	Yes	No
RW-7	0.03	0.10	150–1900	Yes	Yes
RW-19	0.03	0.10	150–1900	Yes	Yes
OPC	0.036	0.03	200–5500	No	No
FPC	0.05	0.03	200–5500	No	No



Fig. 4. Material samples tested.

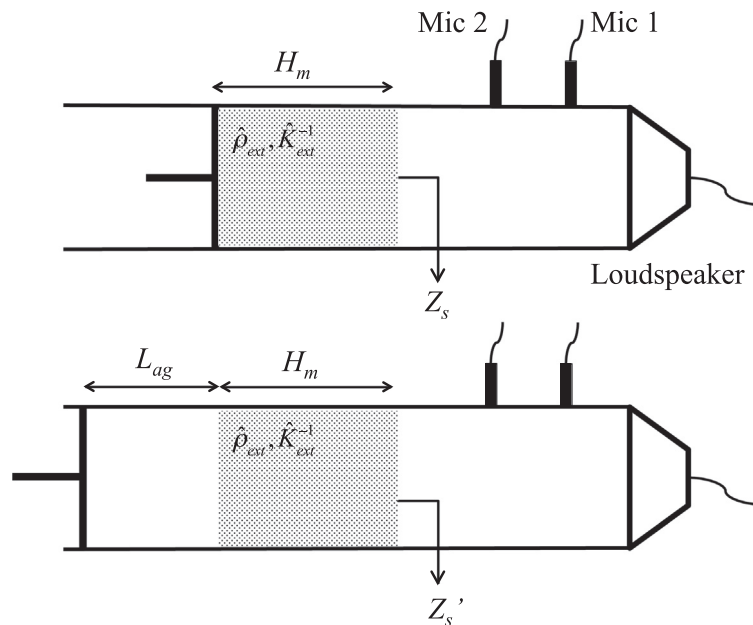


Fig. 5. Kundt's tube configuration in TFM [24] corresponding to two different boundary conditions at the rear face of the sample: (a) rigid backing, (b) an air gap L_{ag} .

sample (RW-19) contain respectively 7 and 19 cylindrical perforations. The diameter of the perforations is 8 mm. The samples were tested in a large Kundt's tube ($D = 100$ mm).

(c) We have also considered two samples of rigid 3D-printed porous networks consisting of cubic periodic cells [40,41,26,42]. The first sample (OPC, one-pore-cell) contains one centered spherical pore per unit cell, connected to the adjacent cell pores through six cylindrical channels. It has a cell size of 3 mm and is composed of 12 cells across the sample thickness (total sample thickness of 36 mm) and 10 cells across the sample diameter. The second material sample (FPC, four-pore-cell) is also formed of periodic cubic cells, but it contains four pores of different sizes per cell, and it is anisotropic. It has a cell size of 5 mm and is composed of 10 cells across the thickness (total sample thickness of 50 mm) and 6 cells across the sample diameter. They have been tested in a small Kundt's tube ($D = 30$ mm). The material consists of ABS polymer filaments Z-ultra (Zortrax M200), with a Young modulus of about 1.85 GPa. Note that the actual Young modulus and Poisson ratio of the porous networks are necessarily lower due to the presence of the pores. The rigidity of the samples suggest however that their Young modulus is still much larger than the melamine and rock wool samples.

The diameter of the samples was very close to the diameter of the tube. In the case that the sample wasn't rigidly fixed on its own, we added an additional layer of tape around the perimeter of the sample to assure so. The only case in which this was necessary was the 3D-printed porous networks.

Table 1 shows the properties of the various material samples used, and Fig. 4 shows pictures of the samples.

4.2. Experimental determination of the extended equivalent fluid using TFM

The extended effective density and compressibility of the material samples are obtained experimentally using TFM. They are determined from two surface impedance measurements corresponding to different boundary conditions at the rear of the sample, namely two different air gaps between the sample and a rigid wall. The setup in the Kundt's tube for the two air gaps is shown in Fig. 5. The details of the method have been included in Appendix A.1. The result is independent, in theory, of the chosen air gaps. In practice there is a restriction at low frequencies: both the distance between microphones and the difference between the two air gap depths need to be sufficiently high to capture the phase differences. Sensibly smoother results are in general obtained when one of the air gaps is set to zero. All results presented, unless explicitly stated, have been obtained using air gaps of $L_{ag} = 0$ and 20 mm for the melamine and 3D-printed samples (small Kundt's tube), and of $L_{ag} = 0$ and 60 mm for the rock wool samples (large Kundt's tube). In all cases the absorption coefficient is shown at the training case $L_{ag} = 0$ mm and at the prediction case $L_{ag} = 40$ mm.

Table 2
JCAL parameters of the various samples obtained from the direct JCAL identification (JCAL).

Porous material	ϕ	α_∞	Λ (m)	Λ' (m)	k_0 (m ²)	k_0' (m ²)	σ (N·s·m ⁻⁴)
Melamine	0.99	1.0	$1.3 \cdot 10^{-4}$	$1.6 \cdot 10^{-4}$	$4.0 \cdot 10^{-9}$	$4.0 \cdot 10^{-9}$	4500
RW	0.99	1.0	$2.4 \cdot 10^{-5}$	$3.5 \cdot 10^{-5}$	$4.0 \cdot 10^{-10}$	$1.5 \cdot 10^{-10}$	44600
OPC	0.42	2.1	$3.2 \cdot 10^{-4}$	$1.1 \cdot 10^{-3}$	$1.4 \cdot 10^{-8}$	$2.4 \cdot 10^{-8}$	1500
FPC	0.35	2.4	$2.2 \cdot 10^{-4}$	$1.0 \cdot 10^{-5}$	$9.0 \cdot 10^{-9}$	$5.8 \cdot 10^{-8}$	2000

4.3. JCAPL identification

In the case of porous materials a JCAPL identification may also lead to the underlying rigid-frame porous medium. In order to check this and compare against the method proposed, an acoustics-based JCAPL identification has also been performed for all single-porosity samples, through the surface impedance with and without an air gap. In order to simplify the identification, the Pride contribution to the model has been ignored, reducing to the JCAL model defined through only six parameters. It has been checked *a posteriori* that the refinement by the Pride parameters is below the experimental and modeling error. For generality, the full JCAPL model is presented in appendix A.2.

A more robust identification is obtained if performed in successive steps [43,44]. The porosity (ϕ) and the viscous permeability (k_0) have been determined *a priori* from the low frequency limits:

$$\phi = \lim_{\omega \rightarrow 0} \frac{\rho_0}{H_m \omega} \operatorname{Im} \left(\frac{1}{Z_s^m(\omega)} \right),$$

$$k_0 = - \lim_{\omega \rightarrow 0} \frac{\mu}{\operatorname{Im} \left(\tilde{k}_{ext}(\omega) \tilde{Z}_{ext}(\omega) \right)},$$

where μ is the molecular viscosity of air. The remaining parameters have been determined from the minimization of the difference between the computed and measured surface impedance, Δ , using the *fminsearch* function of MATLAB®:

$$\Delta = \sum_i \left\| Z_s^m(\omega_i) - Z_s^p(\omega_i) \right\|^2 + \left\| Z_{s,ag}^m(\omega_i) - Z_{s,ag}^p(\omega_i) \right\|^2 \quad (24)$$

where $Z_s^m, Z_{s,ag}^m$ are the measured surface impedances without and with air gap, respectively, and $Z_s^p, Z_{s,ag}^p$ are the predicted surface impedances obtained from Eqs. (6) and (7). The JCAL model for $\tilde{\rho}(\omega)$ and $\tilde{K}^{-1}(\omega)$ (Eqs. (30) and (31)) is used to determine $Z_s^p(\omega)$ and $Z_{s,ag}^p(\omega)$.

Table 2 shows the JCAL parameters obtained for all the materials tested (except those with double porosity). Note that the resistivity is directly calculated from the viscous permeability through the definition $\sigma = \mu/k_0$.

5. Validation against conventional and non-conventional porous materials

In this section the method proposed is applied to the samples tested: melamine foam, rock wool, two rock wool samples with double porosity, and two 3D-printed porous networks. We compare the proposed method against an acoustics-based JCAL identification.

Table 3 shows a summary of the results obtained for all the samples, in terms of the poles required to describe the extended equivalent fluid and the poles retained in the equivalent fluid model of the material.

Table 3
Summary of the equivalent fluid characterization of the material samples tested.

Material	JCAL	Pole pairs of $\tilde{\rho}_{ext}$	Pole pairs of \tilde{K}_{ext}^{-1}	Pole pairs of $\tilde{\rho}$	Pole pairs of \tilde{K}^{-1}
Melamine	Yes	1 real	1 real	1 real	1 real
RW	No	1 real + 1 compl-conj	1 real + 1 compl-conj	1 real	1 real
RW-7	No	1 real + 1 compl-conj	1 compl-conj	1 real	no poles
RW-19	No	1 real + 1 compl-conj	1 compl-conj	1 real	no poles
OPC	Yes	1 real	1 real	1 real	1 real
FPC	Yes	1 real	1 real	1 real	1 real

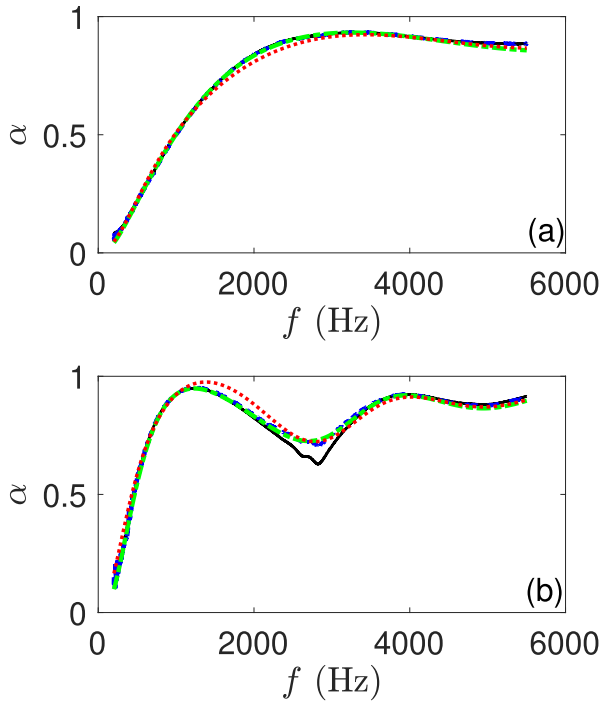


Fig. 6. Absorption coefficient of the melamine sample corresponding to the direct measurement (—), the calculation from the full extended equivalent fluid determined from TFM (---), JCAL identification (· · · · ·), and the reconstruction using one real pole pair (- · - · -), for $L_{ag} = 0$ mm (a) and $L_{ag} = 40$ mm (b).

5.1. Melamine foam

Fig. 6 shows the absorption coefficients of the melamine sample corresponding to $L_{ag} = 0$ mm (a) and $L_{ag} = 40$ mm (b). In this case the reconstruction using 1 real pole pair follows closely the full extended equivalent fluid result, as well as the direct measurement (except around 2800 Hz). The JCAL identification shows also an overall agreement with the direct measurement. The JCAL parameters identified to the measured surface impedance are shown in Table 2, which are consistent with this type of porous material: a porosity and static tortuosity very close to 1, viscous and thermal lengths of the order of 10^{-4} m and viscous and thermal permeabilities of the order of 10^{-9} m².

Fig. 7 shows the extended effective density and compressibility together with their reconstruction using one real pole pair and the JCAL identification. While \tilde{K}_{ext}^{-1} is well captured by both identification approaches, $\tilde{\rho}_{ext}$ is better captured by the proposed method, even if the impact on the absorption coefficient is small.

5.2. Rock wool

Fig. 8 shows the measured absorption coefficient and the predicted absorption coefficients using a full poro-elastic model and the rigid-frame limit prediction (infinite Young modulus), all corresponding to rigid backing. The one-dimensional analytical solution for the case of a rigidly-backed poro-elastic layer is included in Appendix A.3. The air-frame coupling is strongest around the resonance, around 350 Hz. A weaker secondary resonance is appreci-

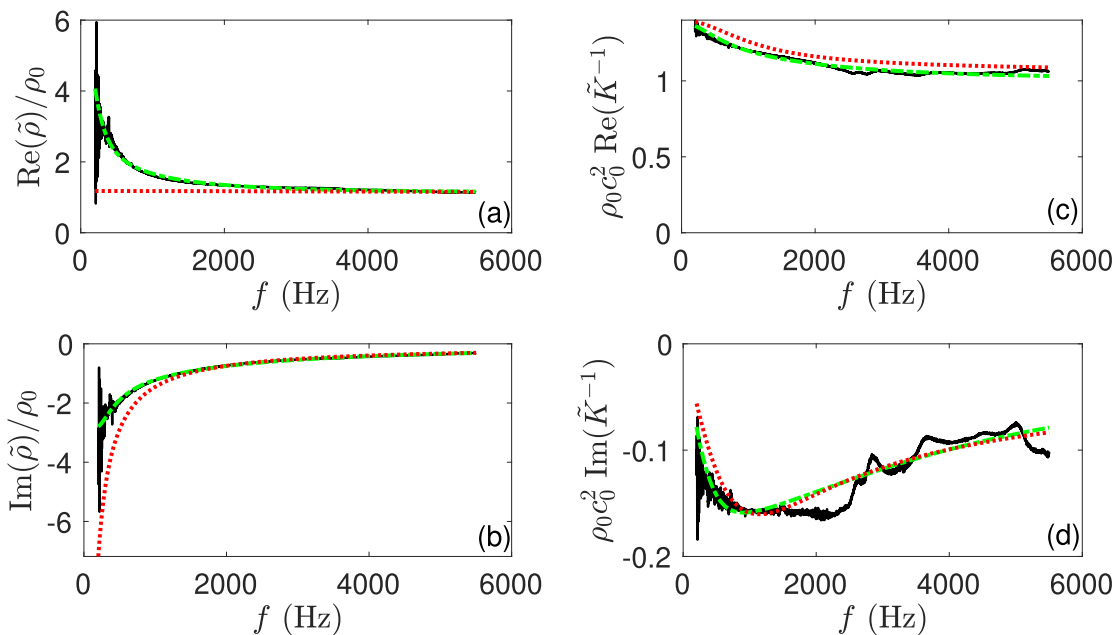


Fig. 7. (a,b) Extended effective density and (c,d) extended effective compressibility of the melamine sample (—), reconstruction using a real pole pair (- · - · -) and JCAL identification (· · · · ·).

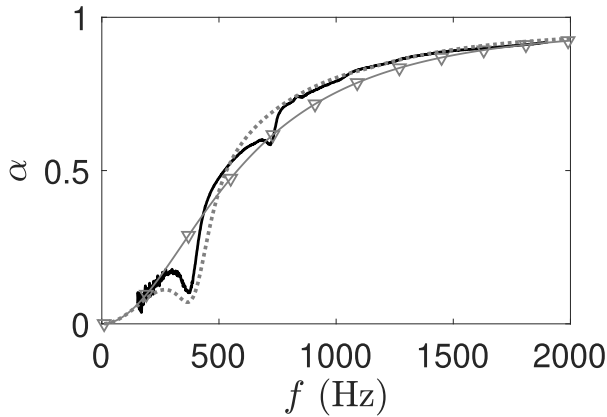


Fig. 8. Absorption coefficient of RW with a rigid backing, measured (—), predicted from a full poro-elastic model (.....), and predicted in the rigid-frame limit $E \rightarrow \infty$ (—▽—).

ated at about 700 Hz. With an air gap the poro-elastic model doesn't predict any resonance (not shown), while the measurements reveal a resonance at about 250 Hz (see Fig. 9(b)). This resonance is thought to be related to a flexural resonance of the sample, not described by the analytical, one-dimensional poro-elastic model.

The measured and predicted absorption coefficients of RW are shown in Fig. 9, corresponding to $L_{ag} = 0$ mm (a,c) and $L_{ag} = 40$ mm (b,d), respectively. Note that in (b) and (d) the prediction from the extended equivalent fluid is extremely accurate, which is the case in all the material samples tested. In (a,b) it is appreciated how the reconstruction using one real pole pair and the JCAL identification both remove the peaks and troughs associ-

ated with the elastic couplings, and follow closely the rigid-frame trend for $L_{ag} = 0$ mm. With the air gap the measurements reveal a flexural elastic resonance at about 250 Hz, whose impact on the acoustic field is accurately predicted by TFM. It is remarkable that the extended effective model based on a single plane wave mode is capable of capturing the effect of such a three-dimensional elastic mode. The reconstruction using a real pole pair is closer to the rigid-frame limit of the full poro-elastic model than the JCAL identification. In (c,d) the measured absorption coefficient and their reconstruction using one real pole pair, one real pole pair plus one complex-conjugate pole pair, and one real pole pair plus two complex-conjugate pole pairs are shown. The first complex-conjugate pole pair describes the effect of the leading elastic resonance, and the second complex-conjugate pole pair describes the second elastic resonance. The sum of both the real and the complex-conjugate pole pairs leads to a precise prediction of the measured surface impedance.

Fig. 10 shows the obtained effective density (a,b) and effective compressibility (c,d). A pair of real poles are enough to capture the underlying rigid-frame behavior, and one complex-conjugate pole pair of $\tilde{\rho}_{ext}$ describes the elastic resonance at 350 Hz. Similar results are obtained for the effective compressibility. While the JCAL identification captures the overall trend, the reconstruction using a pair of real poles is slightly closer to the rigid-frame limit from the full poro-elastic model.

Fig. 11 shows the measured surface impedance around the leading elastic resonance, with the contribution from the real poles of $\tilde{\rho}_{ext}$ and \tilde{K}_{ext}^{-1} subtracted, and is compared against the prediction from the full poro-elastic model, and against a fit of the EMM (Eq. (20)). Figs. 11(a,b) correspond to a rigid backing and 11(c,d) to $L_{ag} = 40$ mm. The prediction from the full poro-elastic model has been obtained by subtracting the surface impedance of the rigid-frame limit ($E \rightarrow \infty$) to the surface impedance of the actual

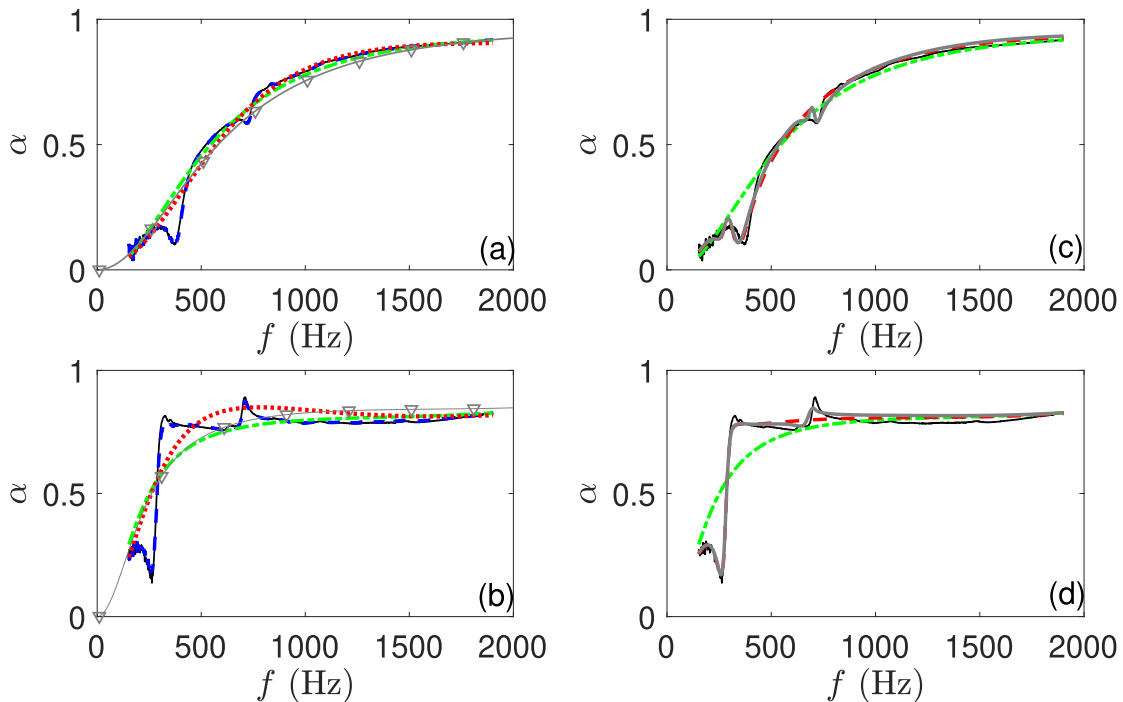


Fig. 9. (a,b) Absorption coefficient of RW corresponding to the direct measurement (—), the full extended equivalent fluid from TFM (■ ■ ■), the reconstruction using one real pole pair (— ▭ —), the JCAL identification (· · · · ·), and the prediction of a full poro-elastic model in the rigid-frame limit, $E \rightarrow \infty$ (—▽—), for $L_{ag} = 0$ (a) and $L_{ag} = 40$ mm (b); (c,d) absorption coefficient of RW corresponding to the direct measurement (—), reconstruction using one real pole pair (— ▭ —), reconstruction using one real pole pair plus one complex-conjugate pole pair for the leading elastic resonance of the sample (· · · · ·), and reconstruction using one real pole pair plus two complex-conjugate pole pairs accounting for both elastic resonances of the sample (—▽—), for $L_{ag} = 0$ (c) and $L_{ag} = 40$ mm (d).

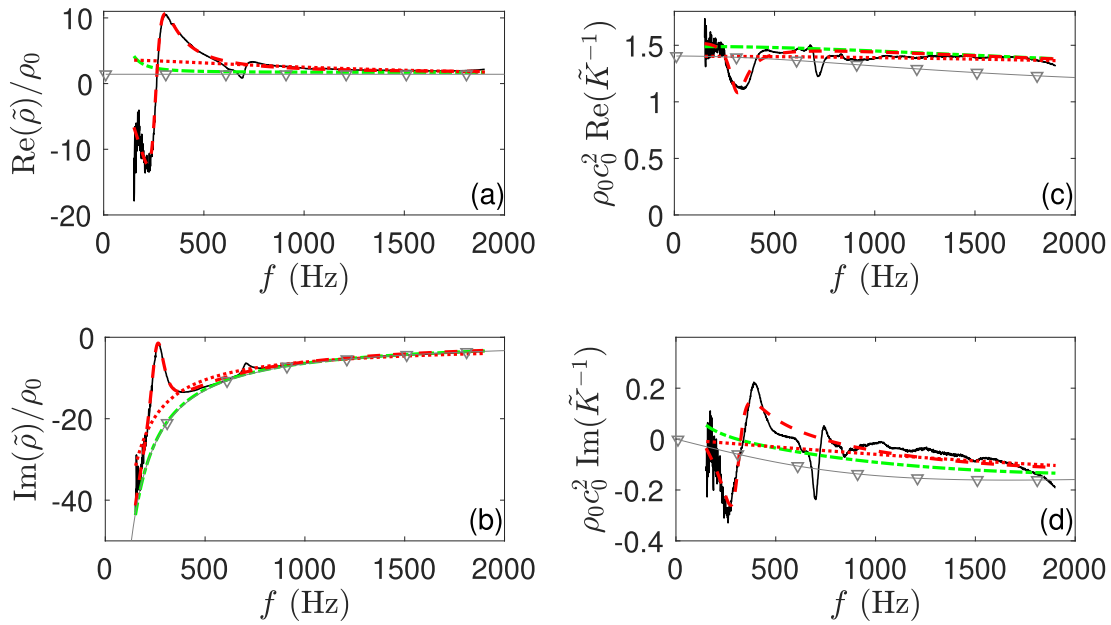


Fig. 10. (a,b) Extended effective density and (c,d) extended effective compressibility of RW (—), reconstruction using one real pole pair (---), reconstruction using one real pole pair plus one complex-conjugate pole pair (---), prediction by the full poro-elastic model in the rigid-frame limit, $E \rightarrow \infty$ (---), and the JCAL identification (.....).

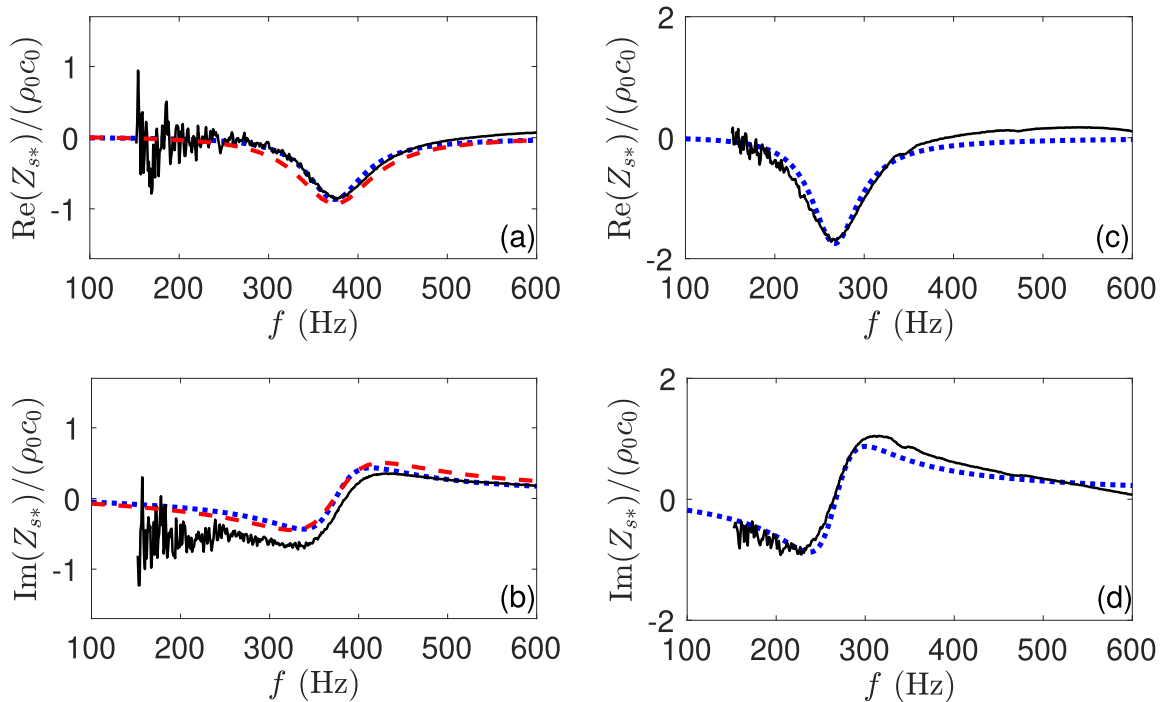


Fig. 11. Surface impedance of RW around the elastic resonance, with the contribution of the real pole pair of $\tilde{\rho}_{ext}$ and \tilde{K}_{ext}^{-1} subtracted, from the measurement (—), the full poro-elastic model (---), and the fit of the EMM (Eq. 20) (.....); (a,b) rigid backing, (c,d) $L_{ag} = 40$ mm.

elastic sample. This is equivalent to subtracting the contribution of the real poles of $\tilde{\rho}_{ext}$ and \tilde{K}_{ext}^{-1} because they account for the rigid-frame behavior. It is observed that the real component is negative, which implies that the EMM requires negative values of m_* , k_* and χ_* . This shows that Z_{s*} cannot be interpreted as an actual surface impedance, but only as a local contribution to the impedance due to the complex-conjugate pole pair of the equivalent fluid. This

peculiar behavior can be used to identify elastic resonances. In the air gap configuration the elastic resonance is flexural and it is thus not captured by the full poro-elastic model, which is one-dimensional. For a rigid backing the measurement trend is well described by both the poro-elastic model and the EMM. A certain bias between the measurement and both models is appreciated at the lowest frequencies. This is attributed to an error in the pole

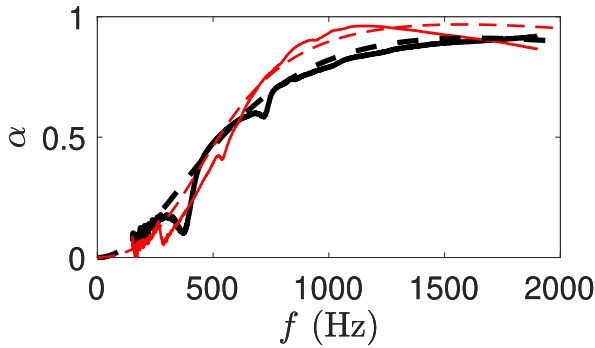


Fig. 12. Measured absorption coefficient of RW-19 (—) and predicted (---), measured absorption coefficient of RW (—) and predicted (---), with a rigid backing.

identification due to the missing of the low-frequency tail of the resonance. With the air gap the EMM model also fits well the measured trend, showcasing its generality.

5.3. Rock wool with perforations: double porosity material

The impact of the air inclusions can be appreciated in Fig. 12, which compares the measured absorption coefficient of RW and RW-19. The predictions using the double porosity model of Olny and Boutin [15] (JCAL for the primary rock wool microstructure and Zwikker and Kosten’s model [45] for the cylindrical air inclusions) are included. Such a coupling model is limited to this simple double-porosity configuration consisting of cylindrical one-dimensional inclusions. Fig. 13 shows the predictions for the effective density and effective compressibility of RW (JCAL, assuming a rigid-frame) and RW with a 10% of perforated surface with air inclusions of 1 mm in diameter. In order to capture the behavior

of the effective density at low frequencies the plots are shown in logarithmic scale. Their reconstruction using one real pole pair are in excellent agreement in the considered frequency range. The reconstructions using only one real pole are also shown. While the proposed method requires in general two real poles, in some cases the contribution of one of the poles is much lower than the other, leading to a good description using a single real pole. This can be appreciated in the present case: for the double-porosity material the effective density is accurately matched using a single real pole, and RW is also matched well by a single pole except at low frequencies.

Fig. 14 shows the absorption coefficient (a,b) and the obtained effective density (c,d) of RW-7. As before, (a) corresponds to $L_{ag} = 0$ and (b) to $L_{ag} = 40$ mm. The absorption coefficients corresponding to the extended equivalent fluid are not shown as they match exactly the direct measurement. This double-porosity sample shows a similar elastic coupling as RW, but at a lower frequency (≈ 280 Hz). Similarly to RW, using one real pole pair plus one complex-conjugate pole pair leads to an accurate reconstruction of the trend corresponding to the complete extended equivalent fluid, with the real pole pair describing the underlying rigid-frame behavior, and the complex-conjugate pole pair describing the elastic sample resonance. In (c,d) it can be observed that the effect of the elastic sample resonance on the effective density is accurately captured by the complex-conjugate pole pair. RW-19 shows similar trends, but with a weaker impact of the resonance (not shown).

5.4. 3D-printed porous material

Contrarily to the previous materials, an important variation of $\tilde{\rho}_{ext}$ and \tilde{K}_{ext}^{-1} of OPC and FPC is observed when changing the air gap pairs used in TFM. In particular, spurious fluctuations in frequency appear for both $\tilde{\rho}_{ext}$ and \tilde{K}_{ext}^{-1} . They can be seen in Fig. 15,

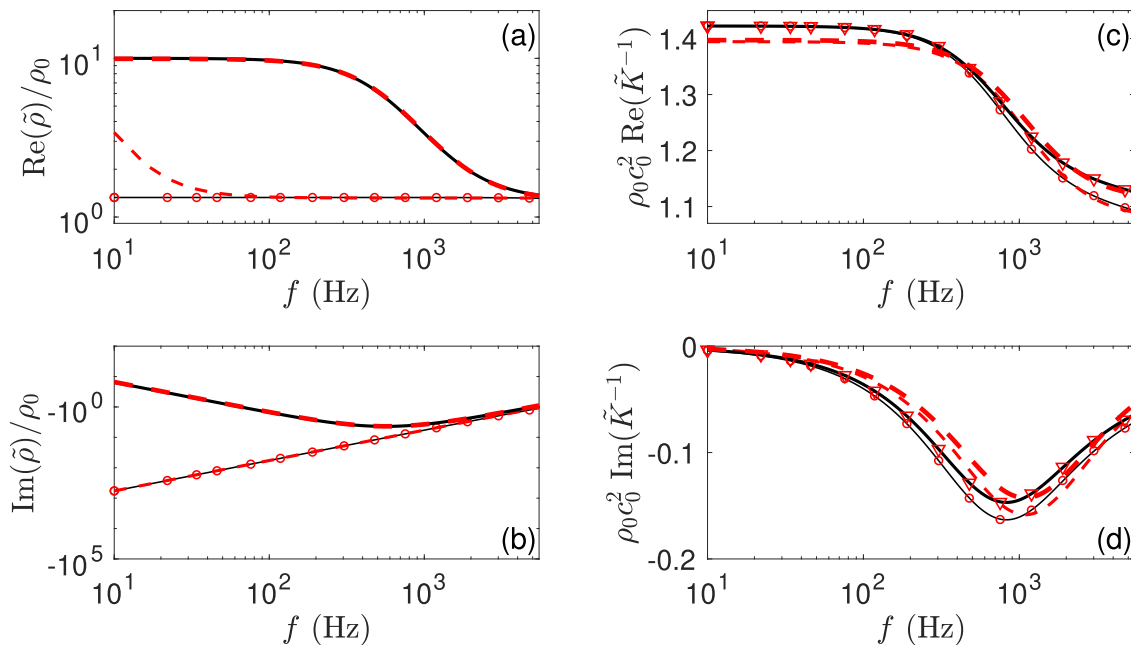


Fig. 13. Effective density (a,b) and effective compressibility (c,d) of RW (rigid-frame) (—), fit of RW with one real pole (---), fit of RW with two real poles (○), RW with a double porosity of 10% of perforated surface (—), fit of RW with a double porosity of 10% of perforated surface using one real pole (---), and fit of RW with a double porosity of 10% of perforated surface using two real poles (△).

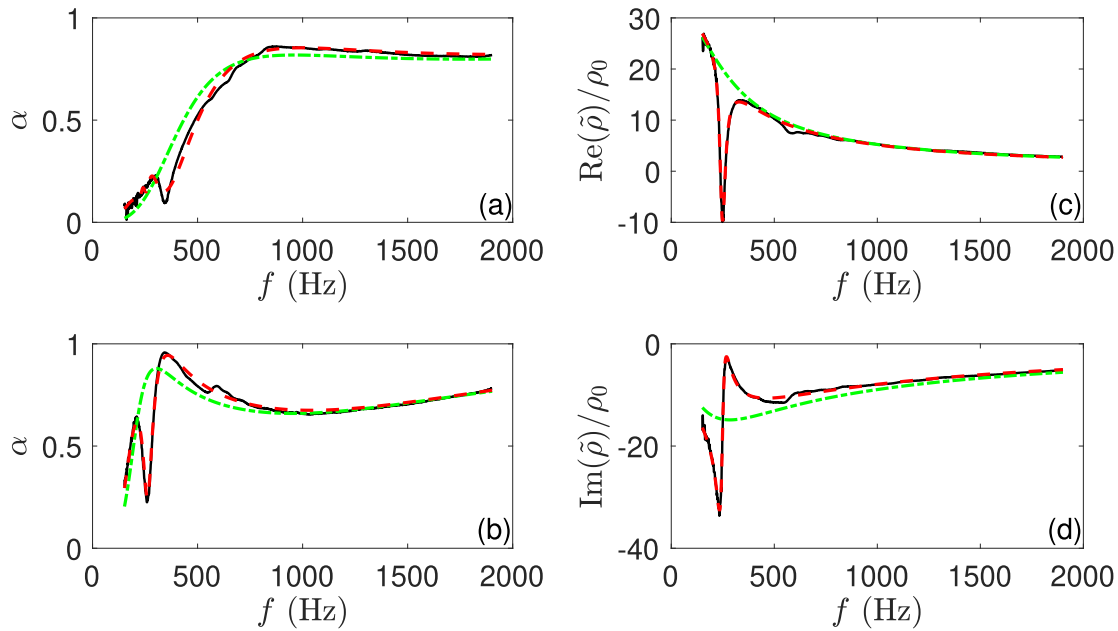


Fig. 14. (a,b) Absorption coefficient of RW-7 corresponding to the direct measurement (—), a reconstruction using one real pole pair of $\tilde{\rho}_{ext}$ and no real poles of \tilde{K}_{ext}^{-1} (— · — · —), and a reconstruction using two real poles plus a complex-conjugate pole pair for $\tilde{\rho}_{ext}$ and two complex-conjugate pole pairs for \tilde{K}_{ext}^{-1} (- - -), for $L_{ag} = 0$ (a) and $L_{ag} = 40$ mm (b); (c,d) measured extended effective density (—), reconstruction using a real pole pair (— · — · —) and reconstruction using a real pole pair plus a complex-conjugate pole pair (- - -).

which displays $\tilde{\rho}_{ext}$ for two pairs of air gaps, together with its reconstruction using one pair of real poles. The reconstructions using one

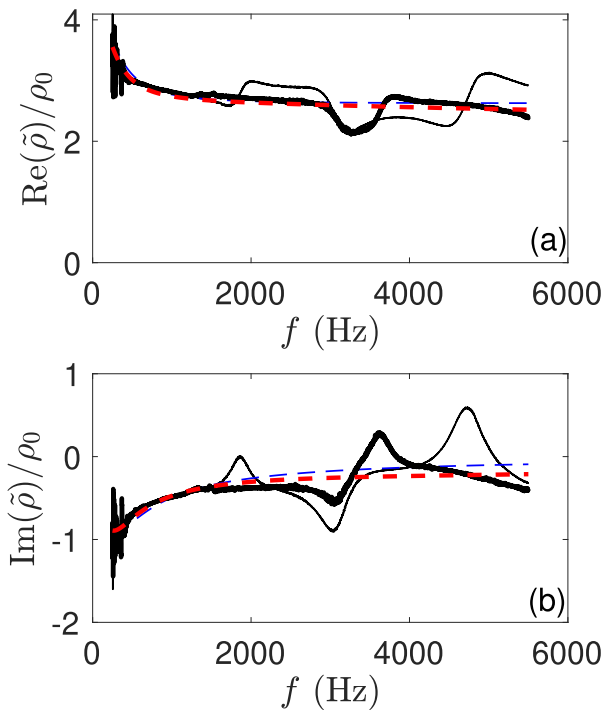


Fig. 15. Extended effective density of OPC corresponding to $L_{ag} = 0$ and 20 mm (—), $L_{ag} = 10$ and 20 mm (— · — · —), the reconstruction of the former (- - -) and the latter (- - -) using one real pole pair.

real pole pair are close to each other, indicating that they are more robust to changes in the air gaps, thus providing a consistent model for the equivalent fluid of the material. The oscillations observed in $\tilde{\rho}_{ext}$ and \tilde{K}_{ext}^{-1} are interpreted as spurious fluctuations due to the failure of the plane wave approximation in these samples, due to the limited ratio of the sample thickness to the pore size (~ 10).

The absorption coefficients of OPC are shown in Figs. 16(a,b), corresponding to $L_{ag} = 0$ (a) and $L_{ag} = 40$ mm (b). With a rigid backing, the absorption coefficients from both the JCAL identification and the reconstruction of $\tilde{\rho}_{ext}$ and \tilde{K}_{ext}^{-1} using one real pole pair mimic closely the direct measurement. On the other hand, for the prediction case $L_{ag} = 40$ mm the trend corresponding to the full extended equivalent fluid obtained from TFM leads to an important error at the largest frequencies, while both the JCAL identification and the reconstruction with one real pole pair predict accurately the direct measurement. This shows that 1) this material obeys closely JCAL when it comes to the surface impedance, and 2) the reconstruction using a pair of real poles is robust to the failure of TFM at high frequencies.

The analogous results for FPC are presented in Fig. 16 (c,d). In this case the predictions of the absorption coefficient at both air gaps are worse in general, with a slightly better agreement coming from the reconstruction using a pair of real poles, especially for $L_{ag} = 40$ mm. This shows that even in such an anisotropic medium the proposed method captures better the behavior than a JCAL identification. Also, the thermal length (Λ_t) obtained from the JCAL identification is in this case smaller than the viscous length (Λ) (see Table 2). This contradicts the physical assumptions of the model and casts doubt on the validity of the identification. On the other hand, it is also possible that this material in particular has a microstructure which is not compatible with JCAL. A complete JCAL identification of the low- and high-frequency asymptotics of this material is required to clarify this issue.

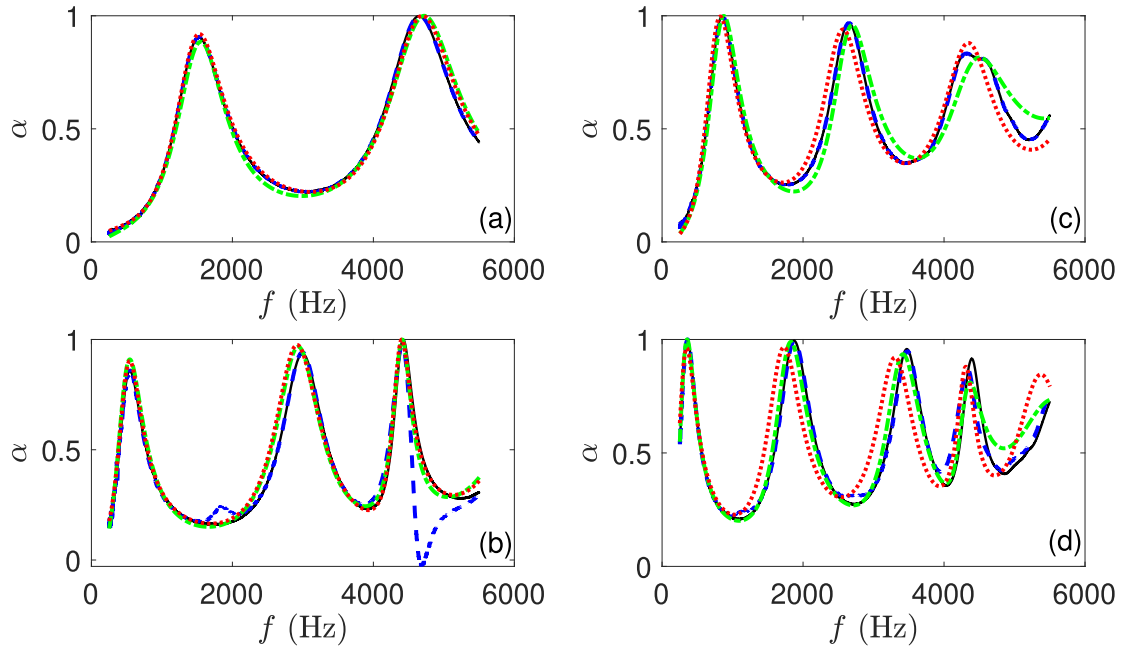


Fig. 16. Absorption coefficient of (a,b) OPC and (c,d) FPC, corresponding to the direct measurement (—), the full extended equivalent fluid (---), the reconstruction using one real pole pair (····) and a JCAL identification (····), for $L_{ag} = 0$ (a,c) and $L_{ag} = 40$ mm (b,d).

6. Conclusions

In this work a new framework to extract experimentally the equivalent fluid of general sound-absorbing materials has been presented, based on a pole identification of the extended effective density and effective compressibility. An extended equivalent fluid can approximate the acoustic response of non-rigid-frame materials (characterized by multiple wave modes propagating in the material) using a single wave mode approximation, and it is estimated from TFM. The proposed method goes beyond the rigid-frame porous materials described by JCAPL, and this has been illustrated by rock wool samples exhibiting an elastic coupling, rock wool samples with double-porosity, and by a sample of 3D-printed network formed of periodic cells of high pore size. An acoustics-based JCAPL identification can also be performed to determine an equivalent fluid of the medium, but the proposed method leads in general to a better agreement with the rigid-frame limit. It appears also that the pole-based identification is robust to local errors of TFM.

One important application of the description of the equivalent fluid using poles is the derivation of a time-domain formulation from Eqs. (1) and (2). Using the additional differential equation method (ADE) [30,46], the equations in the frequency domain can be transformed to an equivalent set of time-domain equations compatible with high-order spatial and temporal schemes. Among others, this opens the possibility of performing high-order, two- and three-dimensional temporal simulations of extended-reacting liners composed of a wide variety of materials.

Declaration of Competing Interest

The authors declare that they have no known competing financial interests or personal relationships that could have appeared to influence the work reported in this paper.

Acknowledgment

This work was performed within the framework of the Labex CeLyA of the University of Lyon, within the program “Investissements d’Avenir” (ANR-10-LABX-0060/ANR-16-IDEX-0005) operated by the French National Research Agency. The authors would like to acknowledge the financial support from the European Union’s Horizon 2020 research and innovation programme through the ARTEM project under grant No 769 350. In addition, the authors would like to thank Tomasz G. Zieliński for providing the 3D-printed samples.

Appendix A. Appendix

A.1. Transfer function method for the determination of the extended equivalent fluid

The extended characteristic impedance and extended propagation wavenumber of the material are determined from a pair of measurements of a single material sample placed in a Kundt’s tube, at two different air gaps, L_{ag}, L'_{ag} , between the rear face of the sample and the rear piston (see Fig. 5):

$$\tilde{Z}_{ext} = \pm \sqrt{\frac{Z_s Z'_s (Z_{ag} - Z'_{ag}) - Z_{ag} Z'_{ag} (Z_s - Z'_s)}{(Z_{ag} - Z'_{ag}) - (Z_s - Z'_s)}}, \quad (25)$$

$$\tilde{k}_{ext} = \frac{1}{j2H_m} \ln \left[\frac{(Z_s + \tilde{Z}_{ext})(Z_{ag} - \tilde{Z}_{ext})}{(Z_s - \tilde{Z}_{ext})(Z_{ag} + \tilde{Z}_{ext})} \right], \quad (26)$$

$$Z_{ag} = -j\rho_0 c_0 \phi \cot\left(\frac{\omega L_{ag}}{c_0}\right), \quad Z'_{ag} = -j\rho_0 c_0 \phi \cot\left(\frac{\omega L'_{ag}}{c_0}\right). \quad (27)$$

The surface impedance at both air gaps are determined from the transfer function of the two microphone signals:

$$Z_s = j\rho_0 c_0 \phi \frac{-H \sin(\omega L_{m1}/c_0) + \sin(\omega L_{m2}/c_0)}{H \cos(\omega L_{m1}/c_0) - \cos(\omega L_{m2}/c_0)}, \quad (28)$$

$$Z'_s = j\rho_0 c_0 \phi \frac{-H' \sin(\omega L_{m1}/c_0) + \sin(\omega L_{m2}/c_0)}{H' \cos(\omega L_{m1}/c_0) - \cos(\omega L_{m2}/c_0)}, \quad (29)$$

where L_{m1}, L_{m2} are the distances from the sample surface to each microphone, and $H = \hat{p}_{m1}/\hat{p}_{m2}$.

A.2. Johnson-Champoux-Allard-Pride-Lafarge model for the equivalent fluid of rigid-frame porous materials

The Johnson-Champoux-Allard-Pride-Lafarge (JCAPL) semi-phenomenological model characterizes a rigid-frame porous material with eight parameters: the porosity (ϕ), the high-frequency limit of the tortuosity (α_∞), the viscous length (Λ), the thermal length (Λ'), the viscous permeability (k_0), the thermal permeability (k'_0), the static viscous tortuosity (α_0) and the static thermal tortuosity (α'_0):

$$\tilde{\rho}(\omega) = \frac{\rho_0}{\phi} \left(\alpha_\infty + \frac{1}{jX} \left(\sqrt{jMN^2 + b^2} - b + 1 \right) \right), \quad (30)$$

$$\tilde{K}^{-1}(\omega) = \frac{\phi}{\rho_0 c_0^2} \left(\gamma - \frac{\gamma - 1}{C} \right),$$

$$C = 1 + \frac{1}{jX'} \left(\sqrt{jM'(N')^2 + (b')^2} - b' + 1 \right), \quad (31)$$

$$b = \frac{2\alpha_\infty^2 k_0}{\Lambda^2 \phi (\alpha_0 - \alpha_\infty)}, \quad b' = \frac{2k'_0}{(\Lambda')^2 \phi (\alpha'_0 - 1)}, \quad (32)$$

$$X = \frac{\omega \rho_0 k_0}{\mu \phi}, \quad X' = \frac{\omega \rho_0 k'_0 \text{Pr}}{\mu \phi}, \quad (33)$$

$$M = \frac{\omega \rho_0}{\mu}, \quad M' = \frac{\omega \rho_0 \text{Pr}}{\mu}, \quad (34)$$

$$N = \frac{2\alpha_\infty k_0}{\Lambda \phi}, \quad N' = \frac{2k'_0}{\Lambda' \phi}. \quad (35)$$

The JCAL model is obtained from ignoring the Pride contribution: $b = b' = 1$. This determines α_0 and α'_0 as a function of the other six parameters.

A.3. Analytical solution for a rigidly-backed poro-elastic layer

The surface impedance of a rigidly-backed layer of poro-elastic material of bulk modulus E and Poisson ratio ν is given by the following equations [14]:

$$Z_s = -\frac{j}{\phi} \frac{Z_L + FZ'_R}{\tan(k_L H_m) - F \tan(k_R H_m)} \quad (36)$$

$$k_R^2 = \frac{\omega^2}{2(PR - Q^2)} (P\rho_{22} + R\rho_{11} - 2Q\rho_{12} - \sqrt{\Delta}) \quad (37)$$

$$k_L^2 = \frac{\omega^2}{2(PR - Q^2)} (P\rho_{22} + R\rho_{11} - 2Q\rho_{12} + \sqrt{\Delta}) \quad (38)$$

$$F = \frac{\phi_R Z_L}{\phi_L Z_R} \quad (39)$$

$$Z_R = (P + Q\phi_R) \frac{k_R}{\omega}, \quad Z_L = (P + Q\phi_L) \frac{k_L}{\omega} \quad (40)$$

$$Z'_R = \left(\frac{Q}{\phi_R} + R \right) \frac{k_R}{\omega}, \quad Z'_L = \left(\frac{Q}{\phi_L} + R \right) \frac{k_L}{\omega} \quad (41)$$

$$\Delta = (P\rho_{22} + R\rho_{11} - 2Q\rho_{12})^2 - 4(PR - Q^2)(\rho_{11}\rho_{22} - \rho_{12}^2) \quad (42)$$

$$\phi_R = \frac{\omega^2 \rho_{11} - Pk_R^2}{Qk_R^2 - \omega^2 \rho_{12}}, \quad \phi_L = \frac{\omega^2 \rho_{11} - Pk_L^2}{Qk_L^2 - \omega^2 \rho_{12}} \quad (43)$$

$$P = K_b + \frac{4N}{3} + \frac{(1 - \phi)^2 K_f}{\phi}, \quad Q = (1 - \phi)K_f, \quad R = \phi K_f \quad (44)$$

$$K_b = \frac{E}{3(1 - 2\nu)}, \quad K_f = C \quad (C \text{ defined in Eq. (31)}) \quad (45)$$

$$\rho_{11} = \hat{\rho}_{11} - j \frac{a}{\omega}, \quad \rho_{12} = \hat{\rho}_{12} + j \frac{a}{\omega}, \quad \rho_{22} = \hat{\rho}_{22} - j \frac{a}{\omega} \quad (46)$$

$$a = \frac{\mu \phi^2}{k_0} \sqrt{1 + \frac{j4\rho_0 \omega \alpha_\infty^2 k_0}{\mu \Lambda^2 \phi^2}} \quad (47)$$

$$\hat{\rho}_{11} = \rho_1 + \phi \rho_0 (\alpha_{\infty-1}), \quad \hat{\rho}_{22} = \phi \rho_0 + \phi \rho_0 (\alpha_{\infty-1}), \quad \hat{\rho}_{12} = -\phi \rho_0 (\alpha_{\infty-1}) \quad (48)$$

In the limit $E \rightarrow \infty$, all sample resonances move to infinite frequencies, and Z'_R and k_R go to zero. The surface impedance becomes:

$$Z_s \approx -\frac{j}{\phi} Z'_L \cot(k_L H_m), \quad (49)$$

i.e. the material behaves like an effective medium of impedance Z'_L and effective wavenumber k_L .

References

- [1] Attenborough K. Acoustical characteristics of porous materials. *Phys Rep* 1982;82:179–227.
- [2] Johnson DL, Koplik J, Dashen R. Theory of dynamic permeability and tortuosity in fluid-saturated porous media. *J Fluid Mech* 1987;176:379–402.
- [3] Champoux Y, Allard JF. Dynamic tortuosity and bulk modulus in air-saturated porous media. *J Appl Phys* 1991;70:1975–9.
- [4] Pride SR, Morgan FD, Gangi AF. Drag forces of porous-medium acoustics. *Phys Rev B* 1993;47:4964–78.
- [5] Lafarge D, Lemariniere P, Allard J-F, Tarnow V. Dynamic compressibility of air in porous structures at audible frequencies. *J Acoust Soc Am* 1997;102:1995–2006.
- [6] Wilson DK. Simple, relaxational models for the acoustical properties of porous media. *Appl Acoust* 1997;50:171–88.
- [7] Horoshenkov KV, Hurrell A, Groby J-P. A three-parameter analytical model for the acoustical properties of porous media. *J Acoust Soc Am* 2019;145:2512–7.
- [8] ISO 9053: Acoustics – materials for acoustical applications – determination of airflow resistance; 1991.
- [9] Champoux Y, Stinson MR, Daigle GA. Air-based system for the measurement of porosity. *J Acoust Soc Am* 1991;89:910–6.
- [10] Allard JF, Castagnede B, Henry M, Lauriks W. Evaluation of tortuosity in acoustic porous materials saturated by air. *Rev Sci Instrum* 1994;65:754–5.
- [11] Biot MA. Theory of propagation of elastic waves in a fluid-saturated porous solid. i. low-frequency range. *J Acoust Soc Am* 1956;28:168–78.
- [12] Biot MA. Theory of propagation of elastic waves in a fluid-saturated porous solid. ii. higher frequency range. *J Acoust Soc Am* 1956;28:179–91.
- [13] Biot MA. Generalized theory of acoustic propagation in porous dissipative media. *J Acoust Soc Am* 1962;34:1254–64.
- [14] Allard JF, Atalla N. Propagation of sound in porous media: Modelling sound absorbing materials. 2 ed. Chichester, West Sussex: John Wiley & Sons; 2009. p. 90.
- [15] Olny X, Boutin C. Acoustic wave propagation in double porosity media. *J Acoust Soc Am* 2003;114:73–89.
- [16] Liu Z, Zhang X, Mao Y, Zhu YY, Yang Z, Chan CT, Sheng P. Locally resonant sonic materials. *Science* 2000;289:1734–6.
- [17] Liu Z, Chan CT, Sheng P. Analytic model of phononic crystals with local resonances. *Phys Rev B* 2005;71:014103.
- [18] Sheng P, Mei J, Liu Z, Wen W. Dynamic mass density and acoustic metamaterials. *Physica B* 2007;394:256–61.
- [19] Lee SH, Park CM, Seo YM, Wang ZG, Kim CK. Acoustic metamaterial with negative density. *Phys Lett A* 2009;373:4464–9.
- [20] Romero-Garcia V, Krynkin A, Garcia-Raffi L, Umnova O, Sanchez-Perez J. Multi-resonant scatterers in sonic crystals: Locally multi-resonant acoustic metamaterial. *J Sound Vib* 2013;332:184–98.
- [21] Seo YM, Park JJ, Lee SW, Park CM, Kim CK, Lee SH. Acoustic metamaterial exhibiting four different sign combinations of density and modulus. *J Appl Phys* 2012;111.
- [22] Roca D, Yago D, Cante J, Lloberas-Valls O, Oliver J. Computational design of locally resonant acoustic metamaterials. *Comput Methods Appl Mech Eng* 2019;345:161–82.
- [23] Fang N, Xi D, Xu J, Ambati M, Srituravanich W, Sun C, Zhang X. Ultrasonic metamaterials with negative modulus. *Nat Mater* 2006;5:452.

- [24] Utsuno H, Tanaka T, Fujikawa T. Transfer function method for measuring characteristic impedance and propagation constant of porous materials. *J Acoust Soc Am* 1989;86:637–43.
- [25] Ngo TD, Kashani A, Imbalzano G, Nguyen KTQ, Hui D. Additive manufacturing (3d printing): a review of materials, methods, applications and challenges. *Compos Part B: Eng* 2018;143:172–96.
- [26] Opiela KC, Zielinski TG. Adaptation of the equivalent-fluid model to the additively manufactured acoustic porous materials. In: *Proceedings of the 23rd International Congress on Acoustics*. Aachen, Germany: EAA; 2019. p. 1216–23.
- [27] Gustavsen B, Semlyen A. Rational approximation of frequency domain responses by vector fitting. *IEEE Trans Power Delivery* 1999;14:1052–61.
- [28] Horoshenkov KV, Attenborough K, Wilde SNC. Padé approximants for the acoustical properties of rigid frame porous media with pore size distributions. *J Acoust Soc Am* 1998;104:1198–209.
- [29] Joseph RM, Hagness SC, Taflove A. Direct time integration of Maxwell's equations in linear dispersive media with absorption for scattering and propagation of femtosecond electromagnetic pulses. *Opt Lett* 1991;16:1412–4.
- [30] Dragna D, Pineau P, Blanc-Benon P. A generalized recursive convolution method for time-domain propagation in porous media. *J Acoust Soc Am* 2015;138:1030–42.
- [31] Smith DR, Schultz S, Markoc P, Soukoulis CM. Determination of effective permittivity and permeability of metamaterials from reflection and transmission coefficients. *Phys Rev B* 2002;65:195104.
- [32] Felbacq D, Bouchitté G. Theory of mesoscopic magnetism in photonic crystals. *Phys Rev Lett* 2005;94.
- [33] Auriault J-L, Boutin C. Long wavelength inner-resonance cut-off frequencies in elastic composite materials. *Int J Solids Struct* 2012;49:3269–81.
- [34] Fellah Z, Depollier C. Transient acoustic wave propagation in rigid porous media: a time-domain approach. *J Acoust Soc Am* 2000;107:683–8.
- [35] Dupont T, Leclaire P, Panneton R. Acoustic methods for measuring the porosities of porous materials incorporating dead-end pores. *J Acoust Soc Am* 2013;133:2136–45.
- [36] Li J, Chan CT. Double-negative acoustic metamaterial. *Phys Rev E* 2004;70:055602.
- [37] Shearer JL, Murphy AT, Richardson H. *Introduction to system dynamics*. 1 ed. Reading, Mass: Addison-Wesley Pub. Co.; 1967.
- [38] Tam CKW, Auriault L. Time-domain impedance boundary conditions for computational aeroacoustics. *AIAA J* 1996;34:917–23.
- [39] Fahy F. *Sound and Structural Vibration: Radiation, Transmission and Response*. 1 ed. London: Academic Press; 1985.
- [40] Zielinski TG. Generation of random microstructures and prediction of sound velocity and absorption for open foams with spherical pores. *J Acoust Soc Am* 2015;137:1790–801.
- [41] Zielinski TG. Pore-size effects in size absorbing foams with periodic microstructure: modeling and experimental verification using 3d-printed specimens. In: Sas AVdWP, Moens D, (Ed.), *Proceedings of the International Conference on Noise and Vibration Engineering*, Heverlee, Belgium; 2019, pp. 95–104.
- [42] Opiela KC, Zielinski TG. Microstructural design, manufacturing and dual-scale modelling of an adaptable porous composite sound absorber. *Compos Part B: Eng* 2020;187:107833.
- [43] Sellen N, Galland M-A, Hilbrunner O. Identification of the characteristic parameters of porous media using active control. *8th AIAA/CEAS Aeroacoustics Conference and Exhibit* 2002.
- [44] Atalla Y, Panneton R. Inverse acoustical characterization of open cell porous media using impedance tube measurements. *Canadian Acoust* 2005;33:11–24.
- [45] Zwikker C, Kosten CW. *Sound absorbing materials*. Elsevier; 1949.
- [46] Bellis C, Lombard B. Simulating transient wave phenomena in acoustic metamaterials using auxiliary fields. *Wave Motion* 2019;86:175–94.